Relationship between Growth Faults, Subsidence, and Land Loss: An Example from Cameron Parish, Southwestern Louisiana, USA

Article *in* Journal of Coastal Research · March 2020

DOI: 10.2112/JCOASTRES-D-19-00108.1

Raphael Gottardi
University of Louisiana at Lafayette

Journal of Coastal Research | 00 | 0 | 000–000 | Coconut Creek, Florida | Month 0000

Relationship between Growth Faults, Subsidence, and Land Loss: An Example from Cameron Parish, Southwestern Louisiana, USA

Matthew O'Leary and Raphael Gottardi*

School of Geosciences
University of Louisiana at Lafayette
Lafayette, LA 70504, U.S.A.

www.cerf-jcr.org

www.JCRonline.org

ABSTRACT

O'Leary, M. and Gottardi, R., 0000. Relationship between growth faults, subsidence, and land loss: An example from Cameron Parish, Southwestern Louisiana, USA. *Journal of Coastal Research,* 00(0), 000–000. Coconut Creek (Florida), ISSN 0749-0208.

This study investigates the relationship between faulting, subsidence, and land loss in coastal Louisiana. A methodology that integrates three-dimensional (3D) seismic data, well logs, high-resolution topographic mapping (LIDAR), and historical aerial photography is successfully developed to identify fault-related geomorphic changes in southwestern Louisiana's Chenier Plain. Analysis of a 3D seismic survey and well logs reveals the presence of 10 normal faults that form an east-west graben in the middle of the study area. Well logs were used to further constrain the geometry of the faults. Shallow water well logs were used to map the faults at shallow depth, below the resolution of the seismic survey. Fault traces were extrapolated to the surface by maintaining constant dip and projected on LIDAR data. Elevation profiles derived from the LIDAR were conducted across the different faults, and results show that a distinct difference between the upthrown and downthrown sides of the faults occurs. Historical aerial photographs were used to investigate any change in geomorphology from 1953 to 2017 within the study area. Results reveal the occurrence of water bodies on the immediate downthrown sides of suspected fault traces. These findings suggest that faulting influences and focuses areas where subsidence is happening and subsequent land loss may occur, and detailed understanding of active shallow faulting in coastal areas can be used to identify regions that are at risk of land loss.

ADDITIONAL INDEX WORDS: *Subsidence, coastal erosion, faulting, Chenier Plain, Shallow faulting.*

INTRODUCTION

Southern Louisiana is experiencing rapid subsidence and land loss and a multitude of environmental problems (*e.g.,* Colten, 2016; Day *et al*., 2007). A review of subsidence research in southern Louisiana by Yuill, Lavoie, and Reed (2009) identifies six controlling parameters: (1) tectonics (fault processes and halokinesis), (2) Holocene sediment compaction, (3) sediment loading, (4) glacial isostatic adjustment, (5) fluid withdrawal, and (6) surface water drainage and management (see Yuill , Lavoie, and Reed [2009] and references therein). The complexity associated with subsidence arises from the fact that these processes are not independent of each other and often exert feedback mechanisms, which make the identification of causal mechanisms difficult. Most subsidence-related research in the United States has been focused on the evolution of the Mississippi River Delta (*e.g.,* Blum *et al*., 2008; Cahoon *et al*., 1995; Coleman, Roberts, and Stone, 1998; Day and Giosan, 2008; Day *et al*., 2007; Dixon *et al*., 2006; Dokka, 2006; Dokka, Sella, and Dixon, 2006; Gagliano *et al*., 2003a,b; Gonzáles and Törnqvist, 2006; Jones *et al*., 2016; Meckel, 2008; Meckel, ten Brink, and Williams, 2007; Morton *et al*., 2005; Shen *et al*., 2017; Törnqvist *et al*., 2006, 2008; Wolstencroft *et al*., 2014; Yu, Törnqvist, and Hu, 2012; Yuill, Lavoie, and Reed, 2009). The problem with subsidence studies on the Mississippi River Delta is the complexity of the interrelations between the different subsidence controls, which is why these studies typically focus on only individual processes that may be controlling subsidence at a specific location and period of time (Yuill, Lavoie, and Reed, 2009).

In this paper, the relationship between faulting, subsidence, and land loss is explored focusing on a different geologic setting, the Chenier Plains of SW Louisiana, drawing from a recent detailed investigation (O'Leary, 2018). The study area is influenced by low-energy waves and a microtidal coastline, which provides an opportunity to investigate the relationship between faulting, subsidence, and land loss in a setting less influenced by the sedimentary processes of the Mississippi River than the delta. The study area is located in SW Louisiana, specifically within Cameron Parish, west of Grand Lake, and is part of Louisiana's Gulf Coast (Figure 1). This region has been characterized as part of the Chenier Plain. The Chenier Plain can be classified as a low profile, storm-dominated, microtidal coast, downdrift, and west of the Mississippi River deltaic plain (Owen, 2008). The plain comprises interspersed Holocene sediments resting unconformably on Pleistocene-aged Prairie Terrace deposits (Gould and McFarlan, 1959). Holocene deposits are primarily mudflats capped by marsh with interspersed thin sand and shell-rich ridges called cheniers, meaning place of many oaks (Russell and Howe, 1935). Chenier is derived from the Cajun word for live oak, which is the primary tree species dominating the crest of ridges. These sediments overlie the Beaumont Alloforma-

---

DOI: 10.2112/JCOASTRES-D-19-00108.1 received 29 July 2019; accepted in revision 20 December 2019; corrected proofs received 5 February 2020; published pre-print online 16 March 2020.

*Corresponding author: gottardi@louisiana.edu

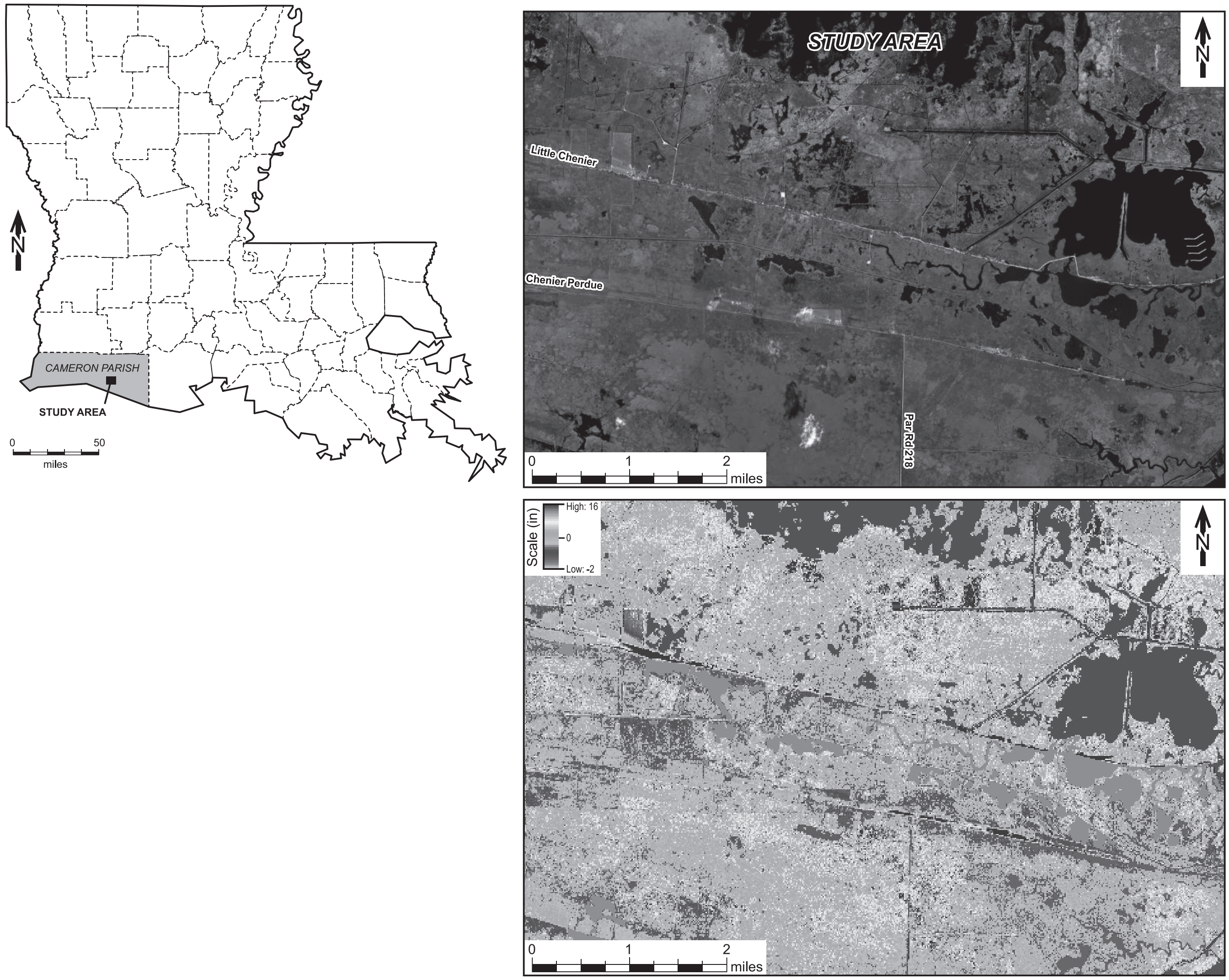

Figure 1. The study area is located in Cameron Parish, SW Louisiana, and covers approximately ~35 square miles. Surface data composed the LIDAR (bottom) and aerial photographs (2017, top) obtained from Atlas Louisiana GIS (2020) and Louisiana State University (LSU): Department of Geography and Anthropology (2020).

tion, which is characterized by Pleistocene-aged fluviatile deposits (Heinrich, 2006; Young *et al*., 2012). Currently, the Chenier Plain of SW Louisiana's Cameron Parish are experiencing high subsidence at ~0.35 in/y (~8.9 mm/y; Nienhuis *et al*., 2017), which is a contributing cause to land loss along the Louisiana coast.

To investigate the relationship between faulting, subsidence, and land loss, analysis of a combination of surface and subsurface datasets is undertaken. An industry three-dimensional (3D) seismic survey is analyzed to delineate shallow faults in the subsurface. Fault traces are then projected to the surface and correlated to surface geomorphology to investigate their influence on coastal subsidence. The LIDAR data and historical aerial imagery are used to confirm the expression of these faults at the surface. The history of fault movement and rates of subsidence was determined through stratigraphy, thickness differentials, and growth index, by using subsurface well log correlation (O'Leary, 2018).

The results of this study constrain the role of faults and subsidence on land loss along the Louisiana coastline in Cameron Parish. The LIDAR elevation data across profiles straddling the fault traces show a vertical difference between the up- and downthrown side ranging from ~1.5 in (38 mm) to as much as 6.6 in (168 mm). Historical aerial photograph from 1953 and 2017 were used to investigate changes in surface geomorphology, revealing the occurrence of water bodies on the immediate downthrown sides of suspected fault traces. The results of this study suggest that faulting plays a strong role in controlling subsidence and possible land loss. The methodology used in this study should be applied along the Louisiana coastline to identify areas of active shallow faulting because they might be at greatest risk of further land loss.

Geologic Setting

The study area is located in the Louisiana Gulf Coast, in Cameron Parish, SW Louisiana. This region has been characterized as part of the Chenier Plain, a low profile, storm-dominated, microtidal coast, downdrift, and west of the Mississippi River deltaic plain, comprising Holocene sediments resting unconformably on Pleistocene aged Prairie Allogroup.

Regional Geology

Sedimentation along the northern margin of the Gulf of Mexico is accommodated by faults that formed during the rifting associated with the breakup of Pangea in the Late Triassic (*e.g.,* Diegel *et al*., 1995; Ewing and Galloway, 2019; Fisk and McClelland, 1959 Galloway, 2008). Increased subsidence, fluctuating sea level, and thermal activity in the Middle Jurassic created conditions favorable for the deposition of the thick Louann Salt in the Gulf of Mexico (*e.g.,* Salvador, 1987). The Gulf of Mexico was eventually flooded by Late Jurassic, and sediments began filling the margins of the basin. Deposition of large quantities of sediments on top of the Louann Salt caused penecontemporaneous fault movement and initiated flowage of the salt and slope mud, thus leading to the development of growth faults (*e.g.,* Bruce 1973; Worrall and Snelson, 1989). These well-documented faults are present all around the periphery of the Gulf of Mexico Basin and exert a primary control of sedimentary processes (*e.g.,* Diegel *et al*., 1995).

The dominant structural features of southern Louisiana, including Cameron Parish where the study area is located, are sizeable down-to-the-south growth faults and include, to a lesser extent, piercement-type salt domes, deep-seated domes, and other fault structures (Antoine and Bryant, 1969; McLean, 1957). The Gulf Coast's relationship with faulting is derived from sediment loading on ancient unstable Late Cretaceous shelf margins (Yang, 1992). Throughout the Cenozoic sedimentation surpassed the rate of subsidence such that there was a seaward shift of depocenters and shelf edge progradation toward the basin (Yang, 1992). Increased sediment loading on the underlying Louann Salt intensified halokinesis, contributing to the development of growth faults (Bruce, 1973). Growth faults generally have an east-west trending strike parallel to subparallel with the shoreline of the Louisiana Gulf Coast (Culpepper *et al*., 2019; McCulloh and Heinrich, 2012; Murray, 1961).

Subsidence

Subsidence is the gradual sinking of an area of land, with respect to some geodetic level (sea level, for example). Subsidence is controlled by natural drivers such as tectonics (faulting) processes, sediment loading and compaction, glacial isostatic adjustment (*e.g.,* Yuill, Lavoie, and Reed, 2009), anthropogenic drivers such as fluid withdrawal, and surface water drainage and management (*e.g.,* Dokka, 2011; Yuill, Lavoie, and Reed, 2009). In the Chenier Plain, the combination of sea-level fluctuations, reduced sediment supply, compaction, and consolidation of sediment through dewatering controls subsidence (Gosselink, Cordes, and Parsons, 1979). Compaction and consolidation play a dominant role. These processes include, for example, consolidation of sediment textural variability; compaction of underlying sediments from weight of levees (both natural and artificial), beaches, buildings, piles and fills; lowering of the water table through extraction of groundwater, salt, sulfur, oil, gas, or reclamation practices; and extended droughts or marsh burning that cause surface dehydration and shrinkage in highly organic soils and oxidation of organic matter (Gosselink, Cordes, and Parsons, 1979).

Some studies attribute subsidence to compaction of Holocene sediments and argue that the Louisiana coast is stable in a vertical sense, and restoration efforts will offset the natural compaction of Holocene sediments (González and Törnqvist, 2006; Törnqvist *et al*., 2006). However, recent studies conducted in the Mississippi River delta plain suggest that subsidence affects not just Holocene sediments but also extends deeper to the Pleistocene sediments (*e.g.,* Armstrong *et al*., 2014; Dokka, 2011; McCulloh and Heinrich, 2012; Yeager *et al*., 2012). In the Chenier Plain, the Pleistocene surface lies only 33 ft (10 m) below the surface, whereas the Mississippi River Delta's Pleistocene surface is 984 ft (300 m) deep (Fisk, 1948; Kulp, 2000). In the past, Gosselink, Cordes, and Parsons (1979) found that the overall net rate of subsidence (or relative sea-level rise) averages 0.69 in/y (17.5 mm/y) on the Chenier Plain. Recently, using data from the Coastwide Reference Monitoring System, Nienhuis *et al*. (2017) found subsidence rates have reduced to 0.35 in/y (8.9 mm/y) in the Chenier Plain based on shallow subsidence rates by taking the difference between vertical accretion of sediment and surface-elevation change.

Growth Faulting Related to Subsidence

Although consolidation and compaction are responsible for subsidence within Holocene sediments, deeper processes such as growth faulting can also contribute (Dokka, 2006). Growth faults propagate upward through thin sedimentary cover (Kuecher, 1995). Kuecher (1994) interpreted seismic sections illustrating evidence of subcropping faults in the Lafourche Delta. These faults, Golden Meadow and Lake Hatch, have been located on seismic surveys, as well as concluded to be active in the Holocene sedimentary section based on core data on both sides of the fault (see review by Culpepper *et al*. [2019] and references therein; Akintomide and Dawers, 2016; Bullock, Kulp, and McLindon, 2019; Frank, 2017; Frank and Kulp, 2016; Johnston *et al*., 2017; Kuecher, 1994; Scates *et al*., 2019; Scates and Zhang, 2019). In some areas of South Louisiana, subcropping growth faults have a causal relationship with new areas of land loss (Kuecher, 1994). Faulting has been linked to tectonic subsidence through geodetic leveling and water gauge observations: Dokka (2006) found that tectonic subsidence accounted for 73% of total subsidence in the Michoud area of Orleans Parish, Louisiana. Benchmarks in the hanging wall of the study area showed 0.39 cm/y of subsidence between 1969 and 1971 and 0.23 cm/y from 1971 to 1977 (Dokka, 2006).This coincided with activation of the Michoud fault, which slipped 0.24 cm/y from 1959 to 1971 and 0.15 cm/y from 1971 to 1977 (Dokka, 2006).

Chenier Plain Sedimentary Environment

In Louisiana, the Northern Gulf of Mexico Basin comprises sediments deposited by several Louisiana drainage systems,

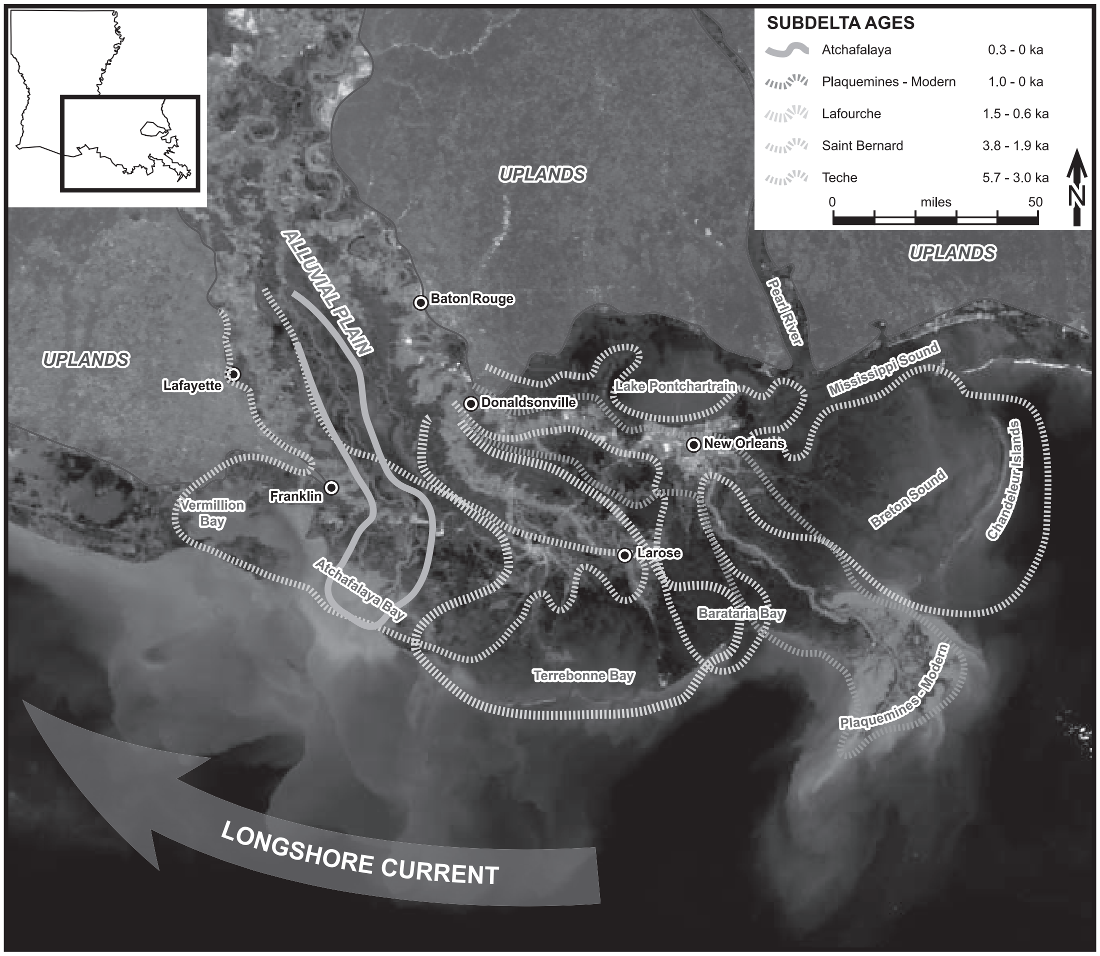

Figure 2. The Mississippi Deltaic plain showing recent subdeltas and associated river and distributary courses. Delta lobe switching has a direct impact in the evolution of the Chenier Plain. As the delta lobe switched to the west (Teche or Lafourche stages), the Chenier Plain received a higher sediment influx, causing the shore to shift seaward. Eastward migration of the delta lobe (Saint Bernard or Plaquemines stages) reduces sediment influx, leading to erosive wave action and formation of new cheniers. Modified Gould and McFarlan (1959) and Fisk (1955).

including the Mississippi and Atchafalaya rivers (Figure 2). The dominant directed longshore current reworks and disperses these delta sediments westward across the coast of Louisiana and Texas (Figure 2; Davies and Moore, 1970; Ellwood, Balsam, and Roberts, 2006; Hijma *et al*., 2017; McBride, Taylor, and Byrnes, 2007; Van Andel, 1960). These sediments are the primary source that contributed to the formation of Chenier Plain paleo-shorelines reworked by wave and storm energy (Figure 3; Gosselink, Cordes, and Parsons, 1979). Bay, lake, and marsh deposits, situated both vertically and laterally to each other, are among other sedimentary environments composing the Chenier Plain (Gosselink, Cordes, and Parsons, 1979). Environments that were once a coastal marsh could quickly become a lake or bay in relatively short intervals of time because of minute changes in rates of sea-level rise and subsidence (Gosselink, Cordes, and Parsons, 1979). Radiocarbon dating of marsh deposits can be used to reconstruct the depositional histories and rates of subsidence of these areas (DeLaune, Baumann, and Gosselink, 1983; Dokka, 2006; Gould and McFarlan, 1959). These near-surface deposits rest upon a seaward-thickening accumulation of gulf-bottom sands and silty clays that compose the upper part of the sedimentary wedge (Figure 3; Gosselink, Cordes, and Parsons, 1979). These deposits are identified by marine fauna, unique sedimentary structures, and absence of organic detritus accumulations. Bay and lake deposits can be distinguished from each other mainly in their exposure to varying degrees of river and tidal influence (Gosselink, Cordes, and Parsons, 1979). Drowning of relict Pleistocene paleovalley formed many of the inland water bodies, for example, East Bay, Sabine Lake, and Calcasieu Lake along the coast and Grand Lake and White Lake located inland from major Gulf connections. Most of the small lakes originated as marsh ponds that enlarged from subsurface or salinity changes that altered the marsh-building process; irregularly shaped lakes typically represent abandoned river or tidal stream courses (Gosselink, Cordes, and Parsons, 1979).

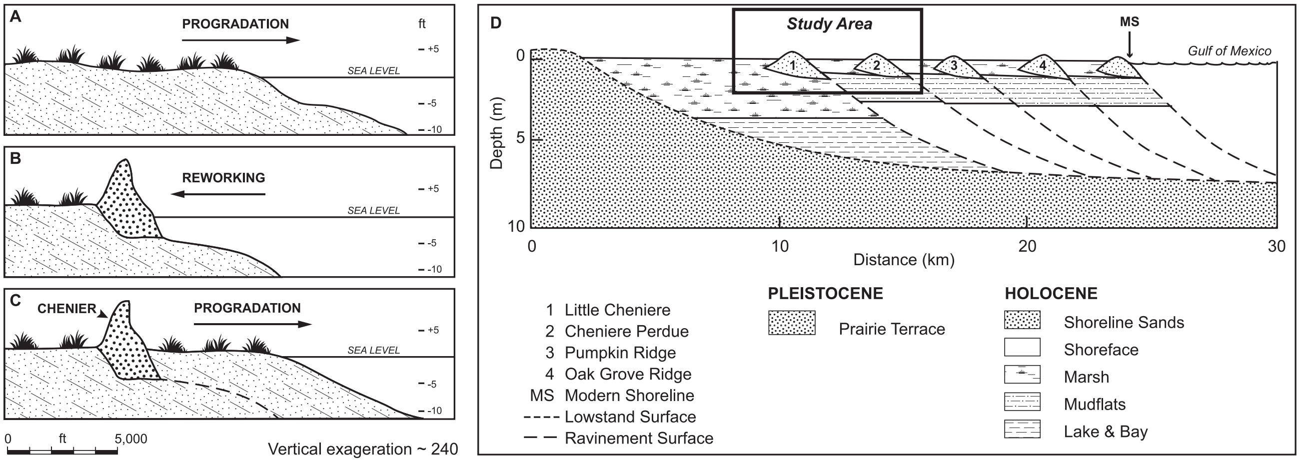

Figure 3. Hoyt's (1969) Chenier Plain process idealized cross section model: (A) mudflat progradation; (B) erosion and reworking of mudflat deposits and formation of ridge along shoreline; (C) mudflat progradation, ridge becomes Chenier. (D) Idealized cross section across Chenier Plain with chronostratigraphic interpretations of facies belts. Cheniers become younger from landward (left) to seaward (right) (modified from Penland and Suter [1989] and Owen [2008]).

Formation

The development of the Chenier Plain stabilized around 3000 years ago as global sea level rose to its present-day level. The Chenier Plain is situated to the south of the coastal prairie region on the coast and spans from Vermilion Bay to Sabine Pass in Texas. To the North, Pleistocene-aged deposits, which form the geologic substrate and upland prairie region of the Chenier Plain region, are found a few kilometers inland from the coast and dip gently into the continental shelf's slope. The formation of the Chenier Plain is directly related to switching of the Mississippi River delta lobe. When the distributary system was more westward, sediment influx was high, and the shore shifted seaward. When the river took a more eastwardly course, erosive wave action reworked sediment into high beach ridges (Figures 2 and 3). The Chenier Plain is thought to have formed by this alternation of suspended sediment deposition and wave erosion of sandy mud, leaving winnowed sand and shells behind (Figure 3; Howe, Russell, and McGuirt, 1935; Russell and Howe, 1935). Extension of the cheniers occurs in areas not actively eroding. Moderate storm surges may build up several meter high chenier, whereas severe storm surges may wash overactive cheniers—producing washover sand deposits accompanying eroded shoreface/dunes. The history of the Chenier Plain has been reconstructed through optically stimulated luminescence and radiocarbon dating combined with aerial photo mosaics, topographic maps, borings, and physiographic analysis (Gould and McFarlan, 1959; Hijma *et al.*, 2017; Penland and Suter, 1989). A wedge of relatively recent sediments recorded the final postglacial sea-level rise and present-day deposits. Progradational Chenier Plain deposits compose the upper part, whereas the basal wedge comprises sediments deposited during a transgressive stage as the sea advanced across the entrenched and subaerial Pleistocene Prairie Terrace, also known offshore and beneath the Chenier Plain as the Holocene-Pleistocene exposure surface (Gould and McFarlan, 1959; Milliken, Anderson, and Rodriguez, 2008). Thin organic clays and peat from this basal unit, which date back to 5600 years ago, rest unconformably on the Prairie Terrace. Optically stimulated luminescence dating of the Beaumont Formation, which forms the Prairie Terrace, in SE Texas has established that it is an amalgamation of high stand deposits, which at its youngest is Marine Isotope Stage 5e through 5a, last interglacial stage, in age (Blum and Price, 1998). Deposition of silty sands and gulf bottom sands and silts topped by brackish marsh and bay deposits signaled the end of transgression and beginning of progradation (Gould and McFarlan, 1959; Penland and Suter, 1989). When the Mississippi River held a more westerly course during the Teche subdelta phase 5.7–3.0 ka (Figure 2), mudflats prograded north of the earliest Chenier Plain shoreline (Hijma *et al.*, 2017). Outbuilding ceased around 2.9 ka when the Mississippi River favored the eastward St. Bernard delta complex (Figure 2), reducing the sediment supply (Hijma *et al.*, 2017). Gould and McFarlan (1959) noted that Pecan Island and Little Chenier are remnants of the first shorelines formed during this period of stability and are the oldest cheniers. Worn conditions of shells and microfauna are evidence of this period's strong wave activity (Gould and McFarlan, 1959). Around 1.2 ka ago, the delta switched to the Lafourche outlet (Figure 2), providing a considerable sediment influx for the Chenier Plain to continue seaward with additional input from Plaquemines and modern-day outlet (Figure 2; Hijma *et al.*, 2017). Changes within the Lafourche delta lobe and temporary distribution through the Plaquemines-Balize (birdsfoot) delta lobe created the majority of the chenier's geomorphology (Gould and McFarlan, 1959; Hijma *et al.*, 2017; McBride, Taylor, and Byrnes, 2007; Penland and Suter, 1989). By 0.3 ka, the Lafourche delta lobe was completely inactive, the and Mississippi River's course was switching to the Plaquemines delta (Figure 2), allowing erosive forces to dominate the Chenier Plain coastline once again.

Internal Stratigraphy

The Chenier Plain comprises alternating coarse clastic ridges and mudflats (*e.g.*, Penland and Suter, 1989). Transgressive sand with reworked shallow marine and brackish shell fauna follows and is topped by coastal dune and sand with root structures and possible marsh paleosol (Figure 3; Owen, 2008). The Chenier Plain extends laterally 200 km from Sabine Pass (Texas) to Vermilion Bay (Louisiana), varying in width between 20 and 30 km with elevations approaching 8 m on the ridges. The Mermentau, Calcasieu, and Sabine rivers run through the complex. Their lakes, Calcasieu and Sabine Lake, dominate the western landscape whereas Grand and White Lake occupy the eastern area of the Chenier Complex. Five major sets of Chenier ridges thicken seaward between 6 and 8 m and are separated by prograding mudflats (Figure 3). These prograding mudflats result from periodic pulses in sediment delivery as the Mississippi River Delta shifted westerly. Stratigraphically, this vast complex can be broken down into distinct cheniers, beach ridges, mudflats, and recurved spits. The facies accompanying the plain reflect that of a beach ridge. They typically are on the eastern updrift side of a distributary and intercept sediments transported by longshore currents. These coarsen upward from fine-grained silt and have foreshore and wash over deposits commonly accompanying their crest. At the base, bioturbation of massive silty sands is common and becomes less prevalent upward. Detrital shells and organic fragments are common. Tropical and winter storms may deposit sand sheets on the shore face or inner shelf. A major progradation during the late Holocene prompted the formation of Little Chenier (dated at 2.9 ± 0.3 ka; Hijma *et al.*, 2017; Figure 3), which represent fluctuations in rates of sea-level rise in addition to changes in the Lafourche delta lobe activity (Figure 2). The study area straddles the Little Chenier (Figure 1).

METHODS

This project combines surface and subsurface data. The subsurface part of this study incorporates proprietary seismic data provided by Seismic Exchange, Inc., on Miami Corporations property and well logs from Strategic Online Natural Resources Information System (SONRIS, 2020) and the Louisiana Department of Natural Resources (DNR; State of Louisiana DNR, 2020). Surface data composed LIDAR and aerial photographs obtained from the Louisiana State University (LSU) Atlas website (Atlas Louisiana GIS, 2020) and LSU's Department of Geography and Anthropology (2020).

Analysis of Seismic Data

The seismic data is housed and interpreted at the DOR Lease Service, Inc., and a detailed interpretation of the volume can be found in O'Leary (2018). The data encompass an area of 35 square miles (Figure 1). The survey's record length is 8 seconds with 2001 samples per trace and a sample interval of 0.004 seconds. The interpretation is limited from 0.3 seconds to 2.7 seconds, which was converted to depth using a velocity survey. The distance between each seismic trace is 82.5 ft (25.1 m). The seismic survey was interpreted using IHS Kingdom (2019). Faults were picked on inlines (seismic line within a 3D survey parallel to the direction in which the data were acquired) from west to east, with 20 traces per skip, to detect large faults and then parsed using two traces per skip along the identified major faults. A crossline (a seismic line within a 3D survey perpendicular to the direction in which the data were acquired) was used to check the interpretation of the faults. The crossline ensures the accuracy of the interpretation and removes erroneous picks. Fault picks are based on visible offsets between strong seismic reflectors. These fault interpretations were picked to the limit of the seismic data depth. Faults that potentially reach the surface, but that become lost in the shallow seismic noise, are stopped where offset is not discernible. A new fault surface is created for these and used to extrapolate where the fault would extend to the surface. These fault picks carry the dip of the deeper surface to ensure consistency across all picks. Based on these interpretations, a total of 10 suspected fault surfaces occur in the study area (Figure 4; O'Leary, 2018). Because of the proprietary nature of the seismic survey, the seismic data interpreted for this investigation cannot be included here.

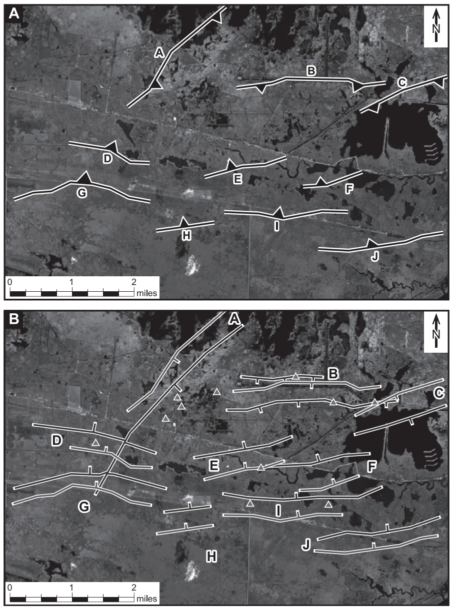

Figure 4. (A) Ten faults were mapped in this study, and fault traces were extrapolated to the surface. (B) Surface fault projections (light gray) and mapped fault trace at 2-seconds depth (dark gray).

Well Log Analysis

Electric, primarily resistivity and spontaneous potential, logs are correlated across several of the faults, using standard techniques of subsurface geologic mapping (see Tearpock and Bischke, 1991). A total of 202 oil and gas, and 45 groundwater wells and historical files, completed between 1937 and 2014, were obtained through the SONRIS website (SONRIS, 2020). Ten electric logs were selected based on their notation of the United States Drinking Water Value, indicating a logged shallow section, and were used for correlation purposes. These well logs are correlated to depths no deeper than 6700 ft (2042 m), the age of which is estimated at approximately Middle Miocene (Paleo Data, Inc., *personal communication*). Main correlations are made between 0 and 2000 ft (0–610 m). Driller logs were obtained from the DNR, ranging from 0 to 800 ft (0–

244 m), with a predominance of logs no deeper than 300 ft (91.5 m), containing lithology description with depth. The notes from the driller logs were converted to a color/lithology pattern corresponding to the description in Excel, then printed and scanned using a log scanner, which allowed them to be depth registered and brought into IHS Kingdom for correlation. Formation tops are assigned based on the log descriptions.

Imagery

Multiple data types are used for the surface investigation in ArcMap. Aerial images, LIDAR, and other georeferenced data are used for the interpretation. Surface fault traces are overlaid on the surface data. Digital elevation models are prepared using ArcMaps 3D Analyst and spatial analyst tools.

LIDAR

The LIDAR data was obtained from Atlas Louisiana GIS (2020). The vertical accuracy of LIDAR digital elevation models (DEMs) is 6 to 12 in (15–30 cm). Subtle changes in the topography, such as fault-related features, can be discerned using LIDAR data (Heltz, 2005). Using the LIDAR DEMs, elevation profiles over areas of interest are done from north to south, perpendicular to the strike of the fault. Data points are exported into an Excel spreadsheet as a graph of the elevation profile. A 98% exponential smoothing factor is added to illustrate the trend and to limit the influence of extreme changes in elevation—abnormal highs or lows are usually associated with roads or canals, respectively. From the LIDAR DEM data, the mean area of the upthrown and downthrown sides of suspected fault surfaces is calculated from zonal statistics.

Aerial Images

Raster data were obtained by collecting and scanning aerial photographs and satellite images (LSU: Department of Geography and Anthropology, 2020). Aerial photographs taken of Cameron Parish from 1953 were used because they displayed the best quality, and they compared effectively to the most recent aerial images (2017). Each image was scanned, imported in ArcMap, and georeferenced using a minimum of four control points.

RESULTS

Analysis of the 3D seismic volume and well logs reveals the presence of 10 normal faults that form an east-west graben in the middle of the study area. Fault traces are extrapolated to the surface and projected on LIDAR data and historical aerial photographs to investigate any geomorphological expression. Elevation profiles derived from the LIDAR data reveal that there is a distinct elevation difference between the upthrown and downthrown sides of the faults. Historical aerial photographs show that between 1953 and 2017, water bodies appeared on the immediate downthrown sides of suspected fault traces. The details of the results are outlined in the following sections.

Faults

Within the study area, detailed analysis of the seismic survey revealed the presence of 10 fault surfaces that were suspected to extend to the surface, labeled A–J (Figure 4). Faults are picked from west to east based on visible offset between horizons, and from the bottom up, to the shallowest interpretable time horizon given the resolution of the seismic data (see Figure 4 for fault trace at the surface and at ~2 s or ~3400 ft/1036 m depth). Faults were then projected to the surface by maintaining constant dip of the fault plane (Figure 5). An error pick was made on the western, central, and eastern portions of the fault as well as a recording of the shallowest or steepest reach of fault picks, defined as ε– and ε+, respectively (see Figure 5), thereby defining a margin of confidence. This margin of confidence was also projected to the surface and was determined to be an average of approximately ±400 ft (122 m) from the projected fault trace (see Figure 5). This error was based on the distance between the last pick-of-confidence angle used to extrapolate the fault surface and zero. Fault surfaces were converted from time to depth (Table 1). All faults are high-angle normal faults. Faults A and C have a NE-SW strike, whereas all other faults strike E-W. Faults A–C dip to the south, whereas Faults D–J all dip to the north, forming a graben in the center of the study area (Table 1, Figure 4). Fault traces at the surface range from 0.88 to 2.40 miles (1.42–3.86 km) in length. Faults B, G, and A are the longest (2.40 [3.86], 2.27 [3.65], and 2.25 [3.62] miles [km], respectively), whereas

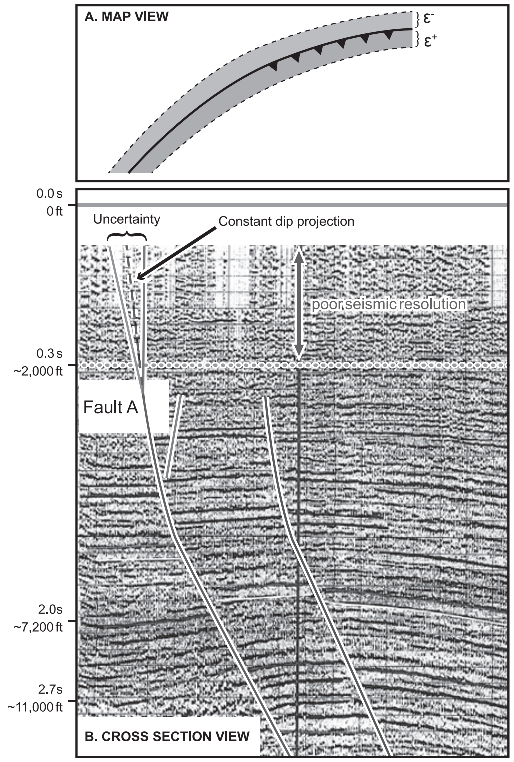

Figure 5. Example of fault in seismic data. Faults are picked as shallow as the seismic resolution allows it. The fault trace is then projected to the surface maintaining constant dip, and the fault can be traced on a map view. However, the dip of the fault falls within a dip uncertainty window, which, when projected in map view, defines two error measurements: the error on the upthrown (ε–) and downthrown side (ε+) of the fault, respectively. Seismic slice adapted from Martin (2006), not to scale, used as reference only.

Table 1. *Fault depths and margin of confidence error.*

Fault	Depth (ft) and (s)						Error ε– (ft)	Error ε+ (ft)
	East		Central		West			
A (top)	–2100	0.613	–1040	0.296	–1710	0.492	395	189
A (bottom)	–10,800	2.688	–8980	2.296	–10,610	2.625		
B (top)	–1840	0.530	–1450	0.416	–2300	0.676	357	287
B (bottom)	–6300	1.724	–6500	1.766	–8600	2.227		
C (top)	–1690	0.482	–3177	0.539	–1470	0.417	434	209
C (bottom)	–7100	1.934	–9150	2.327	–8800	2.267		
D (top)	–2270	0.655	–2150	0.622	–2750	0.800	605	314
D (bottom)	–3930	1.125	–4860	1.381	–5975	1.667		
E (top)	–2210	0.589	–1730	0.488	–1920	0.556	532	446
E (bottom)	–7140	1.95	–6440	1.748	–5065	1.435		
F (top)	–2002	0.578	–1793	0.514	–1713	0.493	370	200
F (bottom)	–6560	1.780	–6865	1.850	–4938	1.405		
G (top)	–2030	0.592	–2140	0.622	–2600	0.74	539	450
G (bottom)	–10,571	2.617	–9230	2.317	–9400	2.378		
H (top)	–1700	0.486	–1630	0.467	–2035	0.597	403	278
H (bottom)	–8920	2.275	–8980	2.308	–9120	2.322		
I (top)	–1630	0.468	–1540	0.422	–2500	0.698	407	439
I (bottom)	–9490	2.398	–8787	2.258	–7005	1.862		
J (top)	–2463	0.629	–1079	0.526	–2075	0.535	480	347
J (bottom)	–8610	2.219	–9140	2.232	–8900	2.221		

Faults F and H are the shortest (0.88 [1.42] and 1.00 [1.61] miles [km], respectively).

Surface Elevation across Fault Traces

Using the LIDAR DEM, elevation transects were conducted perpendicular to the strike of the projected fault surface trace (Figure 6). The transect elevations were averaged for comparison of the average elevation of the upthrown and downthrown (Table 2). For consistency, the mean elevation of the upthrown and downthrown sides of faults is measured over an area of approximately equal size by drawing polygons using connecting points from the transects and surface fault projection ends (Figure 7). The LIDAR's elevation points were averaged within upthrown and downthrown areas of the faults and indicate the mean elevation of the area on either side of the surface fault projections (Table 2, Figure 7). The vertical accuracy of the points is 6 to 12 in (15–30 cm); 12 in (30 cm) was used as the error for the elevation transects.

Fault A

Fault A's average upthrown elevation is 0.96 ft (29.0 cm), and downthrown is 0.94 ft (28.6 cm). The NE end of the fault is covered by water (Figure 6). Once the area of open water is removed from the polygon, the average elevation becomes 1.32 ft (40.2 cm) and 1.07 ft (32.6 cm) for the upthrown and downthrown sides, respectively.

Fault B

Fault B's average elevation is 1.70 ft (51.8 cm) and 1.40 ft (42.7 cm) for the upthrown and downthrown sides, respectively. The upthrown side of Fault B has the highest elevation within the study area (seen on Transect B3 for example, Figure 6).

Fault C

Fault C's average upthrown elevation is 1.20 ft (36.6 cm), and downthrown is 0.91 ft (27.7 cm). The downthrown side of Fault C is exposed to open water contributing to the lower elevations, in particular Transects C1 and C2 (Figure 6).

Fault D

Fault D's average elevation is 0.44 ft (13.4 cm) and 0.31 ft (9.4 cm) for the upthrown and downthrown sides, respectively. Transect D4 crosses a medium sized pond on the immediate downthrown side of the fault surface trace.

Fault E

Fault E is one of two faults that have a negative offset (downthrown is higher in elevation than upthrown). Several smaller ponds are found in the upthrown side, contributing low elevations reducing the average of the upthrown. Downthrown, a river or stream follows the strike of the fault (Figure 6).

Fault F

This is the second fault that has a negative offset. Fault F's transect F1 and F2 upthrown side is occupied by open water. A medium pond on the west end contributes to the lower elevations on the upthrown side.

Fault G

Fault G has a positive offset of 0.49 ft (14.9 cm), and Chenier Perdue is on the downthrown side (Figure 6).

Fault H

Fault H average elevation of the upthrown area is 1.33 ft (40.5 cm), and downthrown it is 0.93 ft (28.3 cm). Note the presence of open water on the downthrown side of the fault (Figure 6).

Fault I

Fault I's average area elevation is 0.56 ft (17.1 cm) in positive offset between the upthrown and downthrown. The downthrown side of the fault is occupied by canals, ponds, and small lakes (Figure 6).

Fault J

Fault J has a positive offset of 0.16 ft (4.9 cm) between the upthrown and downthrown elevations. The elevation of the upthrown side of the fault varies dramatically from west to

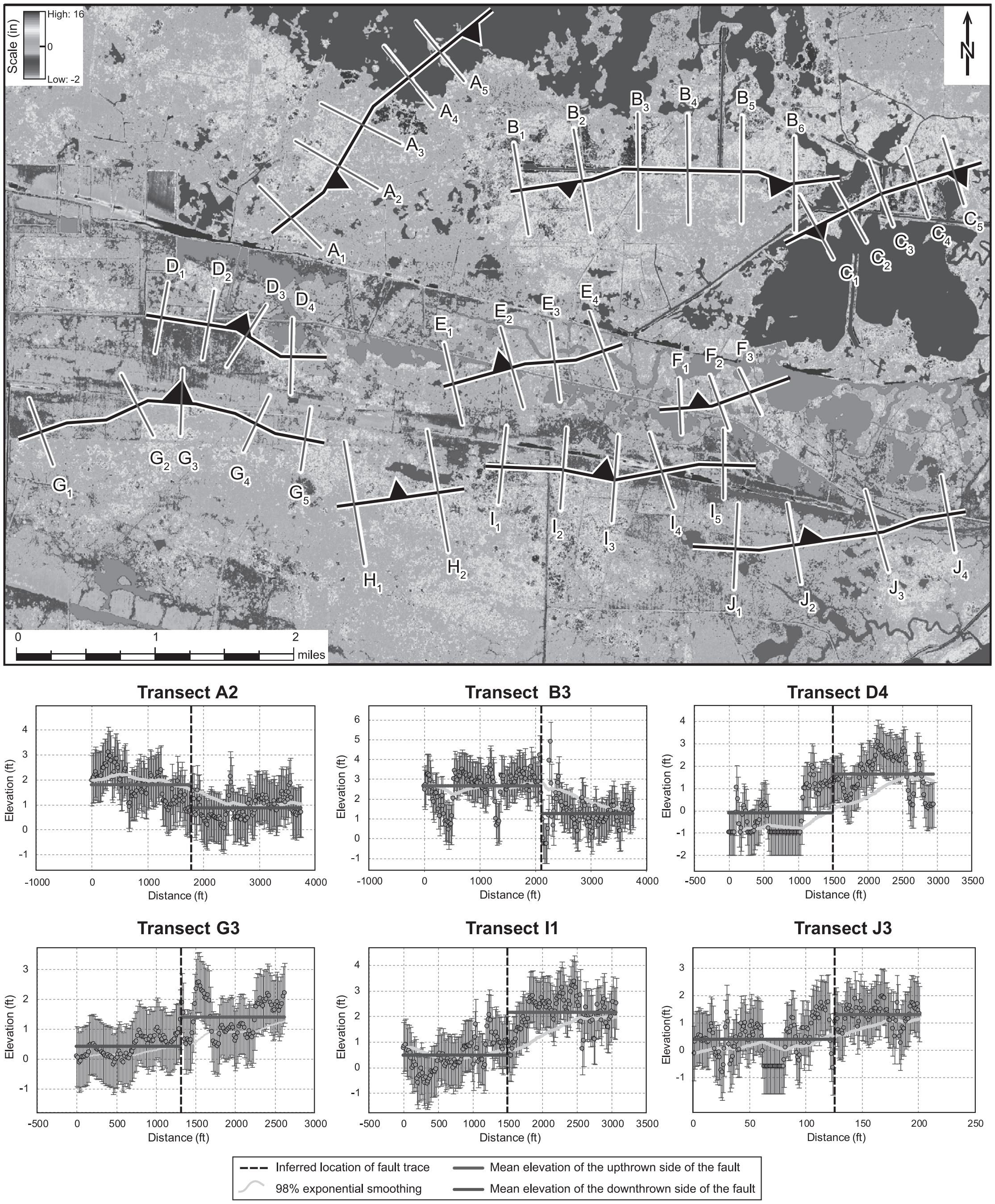

Figure 6. (Top) LIDAR with fault surfaces and transects. (Bottom) Six representative elevation profiles obtained from the LIDAR data, showing the inferred fault location (dashed black line), the upthrown and downthrown sides of the fault, data points, as well as the smoothing average of elevation (light gray line).

east: The eastern extent of the fault is covered by water bodies whereas the western side is much higher. A canal runs through the downthrown side of the fault (Figure 6).

Aerial Photos

A total of 21 aerial photographs were stitched together in ArcMap to show landscape change in the study area between 1953 and 2017 (Figure 8). Fault traces were overlaid on top of the aerial images to investigate their relationship to land surface changes (Figures 8 and 9).

Fault A

Fault A is bounded by cheniers on its southern end (Figure 9). In the 1953 aerial photo, much of the land is scarred by what might be trapper routes and canals. Swamps are present at the NE end of the fault. The vegetation present

Table 2. *Fault surface elevation.*

Transect #	Length (ft)	Average Upthrown Elevation (±1 ft)	Average Downthrown Elevation (±1 ft)
Fault A			
A1	3660	1.46	0.5
A2	3540	1.78	0.85
A3	2880	1.37	0.97
A4	3060	0.12	0.54
A5	2940	0.27	0.86
Average transect Elevation		1	0.74
Average area elevation		0.96	0.94
Fault B			
B1	3540	2.11	1.5
B2	3930	1.79	1.92
B3	4320	2.63	1.23
B4	4270	1.13	1.47
B5	4100	1.99	1.38
B6	3540	2.16	1.02
Average transect Elevation		1.97	1.42
Average area elevation		1.7	1.4
Fault C			
C1	2820	1.39	–0.02
C2	2720	0.81	–0.03
C3	2280	1.46	1.14
C4	2460	1.68	2.01
C5	2745	1.45	1.17
Average transect Elevation		1.36	0.85
Average area elevation		1.2	0.91
Fault D			
D1	2800	0.11	0.47
D2	2720	0.54	0.95
D3	287	0.2	0.36
D4	2920	1.59	–0.14
Average transect Elevation		0.61	0.41
Average area elevation		0.44	0.31
Fault E			
E1	3180	0.43	0.07
E2	322	0.8	0.38
E3	3050	–0.05	0.75
E4	3170	0.21	0.56
Average transect Elevation		0.35	0.44
Average area elevation		0.5	0.64
Fault F			
F1	2120	–0.89	0.91
F2	2210	0.9	0.39
F3	1930	0.61	0.68
Average transect Elevation		0.21	0.66
Average area elevation		–0.03	0.52
Fault G			
G1	2710	0.99	0.14
G2	2700	1.12	0.39
G3	2540	1.38	0.41
G4	2350	1.02	0.58
G5	2480	1.55	0.78
Average transect Elevation		1.21	0.46
Average area elevation		0.95	0.46
Fault H			
H1	4860	0.98	1.26
H2	4760	1.41	0.57
Average transect Elevation		1.19	0.92
Average area elevation		1.33	0.93
Fault I			
I1	3010	2.15	0.45
I2	3160	2.24	0.81
I3	3350	1.6	0.47
I4	3020	0.65	0.59
I5	2670	0.71	0.31
Average transect Elevation		1.47	0.53
Average area elevation		1.12	0.56
Fault J			
J1	3270	0.46	0.89
J2	3120	0.55	0.5
J3	3250	1.29	0.39
J4	2980	0.47	0.32
Average transect Elevation		0.69	0.53
Average area elevation		0.65	0.49

resembles *Spartina Patens* and Roseau Cane (*Phragmitis*, the clump circles). The SW end of the fault ends on the north side of Little Chenier. The 2017 photo shows that the NE area has a lot more open water on the upthrown and downthrown sides of the fault trace (Figure 9). The downthrown side of Fault A is punctuated by small ponds of open water in the 2017 photo (Figure 9).

Fault B

In the 1953 photo, heavily scarred land is present on both the upthrown and downthrown sides of Fault B. More Roseau Cane is found on the southern side of the fault. In the 1953 photo, two treaded tracks south of the central portion of the fault run east-west, suggesting that the marsh is strong enough to support vehicles (Figure 9). The 2017 photo shows ponds on the downthrown side of the fault, especially on the eastern side (Figure 9). A canal runs serendipitously directly along the strike of the fault (Figure 8).

Fault C

There is dramatic land change associated with Fault C between 1953 and 2017. The 1953 photo shows scarred land on the upthrown side of Fault C (Figure 9). To the south, downthrown of the fault, a canal runs east-west. In addition, there is a small bayou/stream/river offshoot south of the Mermentau River (Figure 9). It runs to the SW in a smooth arcuate trajectory till it meets another stream running east-west from the Mermentau River. The 2017 photo shows an immediate difference from the photographs of 1953: A large lake has formed immediately downthrown to Fault C to the south, within the bounds of the stream present in 1953 (Figure 9). This drainage pattern is subparallel to the surface fault. To the south of Fault C, a canal runs north-south, with levees on either side of it. These levees may contribute to preventing sheet flow across the pond.

Fault D

In 1953, land covers both sides of Fault D (Figure 9). Minor marsh scarring is present in the west. Chenier Perdue is approximately 2000 ft to the south (610 m). There is a large, 60-acre property on the upthrown side of the fault, where two homes and a maintained lawn occupy the rectangular lot of land. The eastern portion of the fault has a considerable amount of variation in vegetation on the downthrown side of the fault. The 2017 photo shows a medium-sized pond on the eastern downthrown side of the fault, where the vegetation appears to have changed from 1953 (Figure 9). The property on the upthrown side appears to be abandoned. A canal that runs

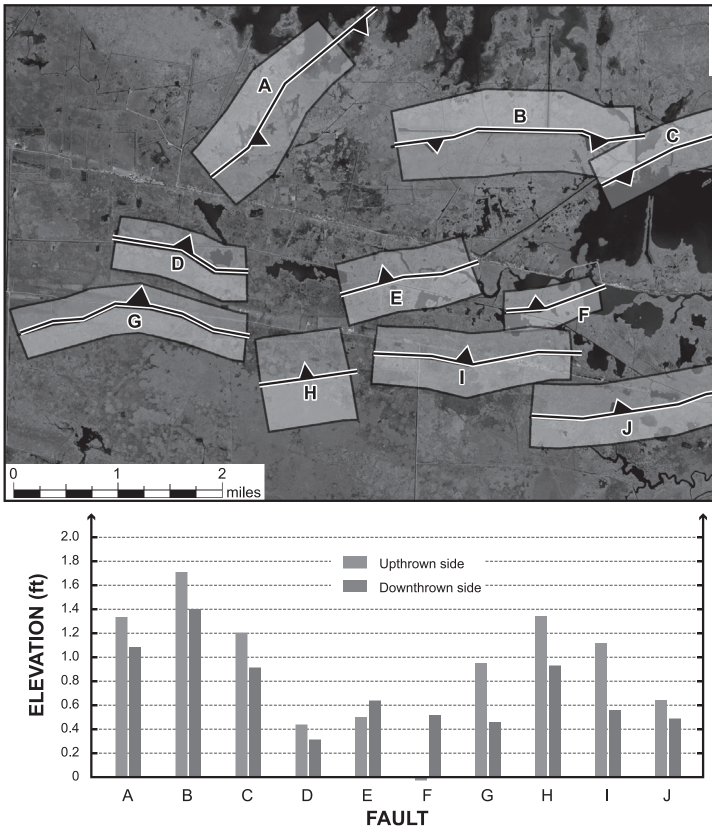

Figure 7. (Top) Map with the polygons used to calculate average elevation on either side of the faults. (Bottom) Histogram comparing the average elevation of the upthrown (light gray) side and downthrown (dark gray) side of the faults. With the exception of Faults E and F, all of the faults show that the average elevation is lower on the downthrown side of the faults.

along the strike of the suspected fault in its western portion, present in 1953, remains.

Fault E

In 1953, the land is heavily scarred on the downthrown side of Fault E (Figure 9). In the east, a river runs along the strike of the fault, deviating to the north when it reaches its center portion. A chenier bounds its NE side. The 2017 photo shows open ponds on both the upthrown and downthrown sides of the fault (Figure 9).

Fault F

In 1953, a large pond can be found 1000 ft (305 m) to the north of Fault F (Figure 9). There is a pond on both the upthrown and downthrown sides in the east. Overall, there is good land coverage. The 2017 photo shows an open pond on the southwest upthrown side of the fault (Figure 9).

Fault G

The downthrown side of Fault G runs along the south side of a chenier. Land is present on both sides of the fault. Large variations in terrains along the chenier can be observed, from varied vegetation, marsh burning, and residential property (Figure 9). No noticeable difference between the upthrown and downthrown side of the fault is seen, however.

Fault H

Land covers both sides of Fault H, and no noticeable difference is seen between 1953 and 2017 (Figure 8). Minor land scarring is observed.

Fault I

In the west, Fault I runs along the south side of the cheniers and crosses over to the north side of the chenier in the east (Figure 8). The 1953 photos show burnt marsh 800 ft (244 m) to the south of the fault (Figure 8). The 2017 photo shows no major difference from 1953.

Fault J

Approximately 1300 ft (396 m) to the north of Fault J, a chenier runs east-west (Figure 8). Marsh was burnt in the west. Minor scarring of the landscape appears on either side. The 2017 photo shows more ragged vegetation. Ponding is present on the downthrown side of the fault, on the shore side of the chenier (Figure 8). To the south on the upthrown side, a stream offshoots from the Mermentau River running east-west.

DISCUSSION

Land loss along the coast of Louisiana is controlled by three main factors: (1) reduced sediment flow from the Mississippi River and its tributaries, (2) sea-level rise, and (3) subsidence

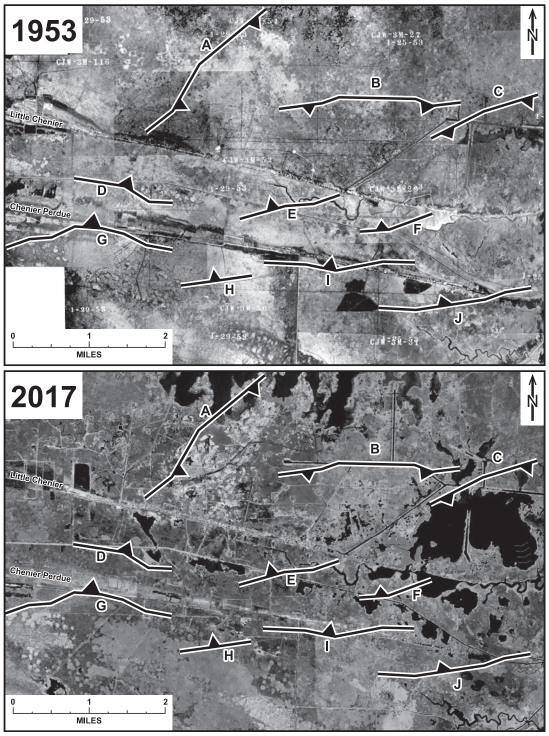

Figure 8. Aerial photograph used to investigate changes in land cover, showing that between 1953 (top) and 2017 (bottom), water bodies appeared on the immediate downthrown sides of suspected fault traces.

(*e.g.,* Chamberlain *et al*., 2018; Zou *et al*., 2015). Reduced sediment flow from the Mississippi River and its tributaries is largely responsible for wetland loss in southeastern Louisiana (*e.g.,* Chamberlain *et al*., 2018; Twilley *et al*., 2016); however, the Chenier Plain represents a different geomorphic environment from the Mississippi River Delta. The Chenier Plain is a low profile, storm-dominated, microtidal coast, down drift, and west of the Mississippi River deltaic plain. It is a sediment-starved area, less influenced by the sedimentary processes of the Mississippi River than the delta, where reduced sediment flow due to river management has been the main factor leading to land loss (Twilley *et al*., 2016). Instead, sediment build up along the Chenier Plain is dependent on longshore drift (Davies and Moore, 1970; Ellwood, Balsam, and Roberts, 2006; Gosselink, Cordes, and Parsons, 1979; Van Andel, 1960). Therefore, the Chenier Plain provides a unique opportunity to study the subsidence mechanisms not linked to sedimentary processes associated with the Mississippi River Delta.

On a longer timescale, sea-level rise poses the greatest threat to Louisiana's coastline (Chamberlain *et al*., 2018; Jankowski, Törnqvist, and Fernandes, 2017). Recent studies suggest that 35% of the wetlands in the Mississippi Delta and 58% in the Chenier Plain may not be able to keep pace with relative sea-level rise (Chamberlain *et al*., 2018). The rate of relative sea-level rise in southern Louisiana is currently between 4 and 20 mm/y, one of the world's highest (Chamberlain *et al*., 2018).

Subsidence related to active growth faulting has largely been understudied (*e.g.,* Dokka, 2006; Dokka, Sella, and Dixon, 2006; Gagliano *et al*., 2003b; Kuecher *et al*., 2001). The Louisiana coastline is riddled with active growth faults, many of which extend to the surface (see recent synthesis of fault traces in SE Louisiana by Culpepper *et al*. [2019] and references therein). Growth faults and fault zones have been documented, but the timing, activity, and slip rates of these faults remains elusive (Dokka, Sella, and Dixon, 2006; Gagliano, 2005; Gagliano *et al*., 2003a,b). Dating fault activity is difficult because it relies on dating of reliable stratigraphic markers. Recent peat chronostratigraphy of Holocene sediments reveals tectonic subsidence rates ranging from 0.1 to 20 mm/y (Dokka, 2006; Gonzáles and Törnqvist, 2006; Kulp *et al*., 2002; Törnqvist *et al*., 2006). At the surface, displacement of geomorphic structures, such as hillslope and river channels,

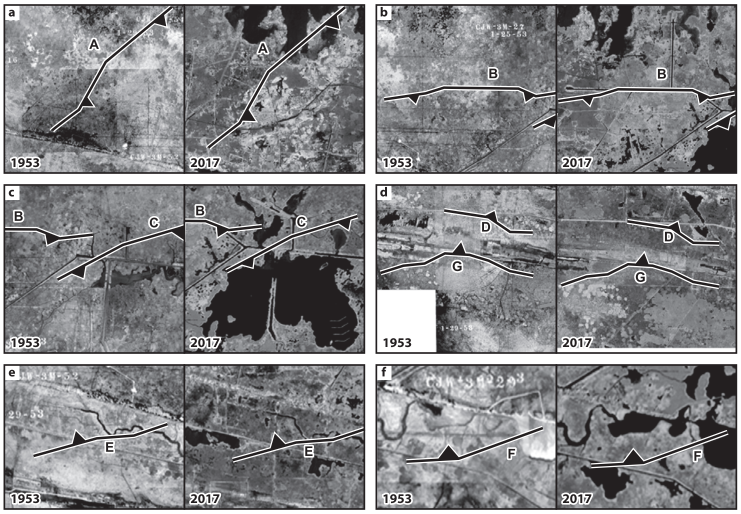

Figure 9. Detail from Figure 8 highlighting some of the most significant land changes observed between 1953 and 2017.

has been used as evidence for active faulting along the Louisiana coastline (Gagliano *et al*., 2003b; Heltz, 2005; Kuecher *et al*., 2001). Studying fault activity is complicated because south Louisiana surface faults appear to be aseismic, as displaced sediment likely undergoes continuous creep rather than abrupt slip-generating earthquakes (Yuill, Lavoie, and Reed, 2009). In addition, the shallow, soft Holocene sedimentary cover typically undergoes diffuse plastic deformation, rather than localized relative displacement along a plane. Fault slip is therefore expressed at the surface by a broad slump rather than a discrete scarp (Yuill, Lavoie, and Reed , 2009), thereby creating geomorphic fault signature difficult to identify at the surface for faults with small magnitudes of surface displacement. In the Chenier Plain, the Pleistocene surface lies only 33 ft (10 m) below the surface, whereas the Mississippi River Delta's Pleistocene surface is 984 ft (300 m) deep (Fisk and McFarlan, 1955; Kulp, 2000); therefore, in the study area, the effect of Holocene sediment compaction and creep is likely minimal.

An alternative approach to investigate the control of faulting on subsidence and associated land loss is to use industry seismic data to map faults. In this study, the analysis of a 3D seismic survey allows detailed fault mapping within a ~35-square-mile study area located in the Chenier Plain of southern Louisiana. Analysis of the 3D seismic survey reveals the presence of 10 major faults. These normal faults strike approximately east-west. Three dip to the south and seven to the north, defining an east-west graben that runs nearly in the middle of the study area. The faults were identified in the seismic survey and mapped to the last point of confidence (depth of ~2000 ft/610 m) and extrapolated to the surface by maintaining constant dip. Faults were cross-correlated using well logs for depth <2000ft (<610 m) and water well logs and loggers' notes for depth <300 ft (<91 m).

The LIDAR data over the study area are used to corroborate any relationship between the projected fault traces at the surface and land elevation. The upthrown sides of the faults appear to correlate with the highest elevations across the study area, whereas the lowest elevation is found in the graben structure defined by the oppositely dipping faults (Figure 6). Elevation transects over the LIDAR DEMs reveal that there can be up to 1.5 ft (46 cm) of elevation difference between the up- and downthrown side of some faults (Figure 6). Elevation also varies along the strike of the fault. For example, the downthrown side of Fault B is lowest in its middle section, which matches the typical displacement profile expected for a constant fault length normal fault (*e.g.,* Nicol *et al*., 1996). Alternatively, some faults show more variable elevation profiles (Fault J, for example), suggesting that if faults affect surface topography, then displacement is diffuse and is expressed by broad slumps in the less compacted Holocene sediments. Altogether, these observations suggest that a correlation exists between land elevation and the location of the projected fault traces at the surface.

The surface difference observed in the vicinity of the fault traces is perhaps even more dramatic when superposing the fault traces on aerial photographs from 1953 to 2017. In the 1953 aerial photo, it is interesting to note that several streams, tributaries to the Mermentau River, run in the middle of the graben defined by the faults (Figure 8). These streams run approximately west to east, in the same direction as the average strike of the faults. This observation suggests that the drainage system developed on top of the preexisting graben structure, indicating that faulting and associated subsidence controls the hydrology of the area. On the 1953 aerial photograph, only a few water bodies are present, but all of them are located on the downthrown side of faults (Faults C and J, for example; Figure 8). The 2017 aerial photograph highlights the severity of land loss in this area of Louisiana (Figure 8). Areas that were occupied by water bodies are now much larger, such as the downthrown side of Fault C, for example, which is currently occupied by a large (~1.3 square miles) pond (Figure 8). Water bodies are more numerous in the graben structure, especially in the east of the study area. Water has also crept in the north in the vicinity of Fault A, transforming the swamps of 1953 into open water. Generally, across the study area, the appearance of water bodies between 1953 and 2017 is obvious. Faults A, D, E, F, H, and J are all now associated with water bodies that were either nonexistent or much smaller in 1953. Faults E and F notwithstanding, these faults generally had positive offset between their upthrown and downthrown elevation areas, suggesting that faulting might still be active today, controlling subsidence and associated land loss. The comparison between the 1953 and 2017 aerial photograph also highlights significant vegetation changes that are, however, difficult to quantify.

The relationship between subsidence, compaction, sedimentation, sea level, salinity, vegetation, erosion, and land loss remains complex. However, in the Chenier Plain, a sediment starved area, where sediment loading and compaction are likely insignificant, these results indicate that growth faulting likely plays an important role in controlling subsidence and associated land loss.

CONCLUSION

The results from this study shed light on the understudied interaction between growth faulting, subsidence, and associated land loss in the Chenier Plain of SW coastal Louisiana. To investigate the relationship between growth faulting and subsidence, industry 3D seismic data, well logs, water well logs and loggers' notes, LIDAR data, and historical aerial photographs in a study area located in the Chenier Plain of SW Louisiana are used. Results indicate that 10 deep-rooted growth faults reach the surface and form a west-east oriented graben structure. Fault offset at the surface correlates to LIDAR elevation data. Aerial photographs suggest that this graben structure influences the drainage system and hydrology of the study area. Comparison of aerial photographs from 1953 and 2017 reveal that most of the downthrown sides of the mapped faults are occupied by water bodies and have experienced land loss. The faults reaching the surface are inferred to cause a lowering of ground level on the downthrown side of the faults, contributing to subsidence, and, ultimately land loss.

ACKNOWLEDGMENTS

The authors would like to thank Seismic Exchange, Inc. (SEI), Miami Corporation, and DOR Lease Services, Inc., for providing the necessary data and workspace for this research. Without these assets, this paper would not have been possible. MOL gratefully acknowledges Mr. Chris McLindon for initiating this project and Mr. William Finley for his help.

LITERATURE CITED

Akintomide, A.O. and Dawers, N.H., 2016. Structure of the northern margin of the Terrebonne Trough, southeastern Louisiana: Implications for salt withdrawal and Miocene to Holocene fault activity. *Geological Society of America Abstracts with Programs*, 48(7). doi: 10.1130/abs/2016AM-286148

Antoine, J. and Bryant, W.R., 1969. Distribution of salt and salt structure in Gulf of Mexico: *American Association of Petroleum Geologists Bulletin*, 53(12), 2543–2550.

Armstrong, C.; Mohrig, D.; Hess, T.; George, T., and Straub, K.M., 2014. Influence of growth faults on coastal fluvial systems: Examples from the late Miocene to Recent Mississippi River Delta. *Sedimentary Geology*, 301, 120–132.

Atlas Louisiana GIS. *Maps, downloads, and web services*. https://atlas.ga.lsu.edu/

Blum, M.D. and Price, D.M., 1998. Quaternary alluvial plain construction in response to glacio-eustatic and climatic controls, Texas Gulf coastal plain. *In:* Shanley, K.W. and McCabe, P.J. (eds.), *Relative Role of Eustasy, Climate, and Tectonism in Continental Rocks*. *Society for Sedimentary Geology: Special Publication*, 59, 31–48.

Blum, M.D.; Tomkin, J.H.; Purcell, A., and Lancaster, R.R., 2008. Ups and downs of the Mississippi Delta. *Geology*, 36(9), 675–678.

Bruce, C.H., 1972. Pressured shale and related sediment deformation—Mechanism for development of regional contemporaneous faults. *American Association of Petroleum Geologists Bulletin*, 56(9), 1897.

Bullock, J.S.; Kulp, M.A., and McLindon, C., 2019. An analysis of whether the deep-seated magnolia growth fault in southeastern Louisiana has affected Holocene stratigraphy and geomorphology. *Geological Society of America Abstracts with Programs*, 51(5). doi: 10.1130/abs/2019AM-335641

Cahoon, D.R.; Reed, D.J.; Day, J.W.; Steyer, G.D.; Boumans, R.M.; Lynch, J.C.; McNally, D., and Latif, N., 1995. The influence of Hurricane Andrew on sediment distribution in Louisiana coastal marshes. *In:* Stone, G.W. and Finkl, C.W. (eds.), *Impacts of Hurricane Andrew*. *Journal of Coastal Research*, Special Issue No. 21, 280–294.

Chamberlain, E.L.; Törnqvist, T.E.; Shen, Z.; Mauz, B., and Wallinga, J., 2018. Anatomy of Mississippi Delta growth and its implications for coastal restoration. *Science Advances*, 4(4), eaar4740.

Coleman, J.M.; Roberts, H.H., and Stone, G.W., 1998. Mississippi River delta: An overview. *Journal of Coastal Research*, 14(3), 698–716.

Colten, C.E., 2016. Environmental management in coastal Louisiana: A historical review. *Journal of Coastal Research*, 33(3), 699–711.

Culpepper, D.; McDade, E.; Dawers, N.; Kulp, M., and Zhang, R., 2019. Synthesis of fault traces in SE Louisiana relative to infrastructure. *Tran-SET Project No. 17GTLSU12. Publications*, 30. https://digitalcommons.lsu.edu/transet_pubs/30

Davies, D.K. and Moore, W.R., 1970. Dispersal of Mississippi sediment in the Gulf of Mexico. *Journal of Sedimentary Research*, 40(1), 339–353.

Day, J.W.; Boesch, D.F.; Clairain, E.J.; Kemp, G.P.; Laska, S.B.; Mitsch, W.J.; Orth, K.; Mashriqui, H.; Reed, D.J.; Shabman, L.; Simenstad, C.A.; Streever, B.J.; Twilley, R.R.; Watson, C.C.; Wells, J.T., and Whigham, D.F., 2007. Restoration of the Mississippi Delta: Lessons from Hurricanes Katrina and Rita. *Science*, 315(5819), 1679–1684.

Day, J.W. and Giosan, L., 2008. Geomorphology: Survive or subside? *Nature Geoscience*, 1(3), 156–157.

DeLaune, R.D.; Baumann, R.H., and Gosselink, J.G., 1983. Relationships among vertical accretion, coastal submergence, and erosion in a Louisiana Gulf Coast marsh. *Journal of Sedimentary Research*, 53(1), 147–157.

Diegel, F.A.; Karlo, J.F.; Schuster, D.C.; Shoup, R.C., and Tauvers, P.R., 1995. Cenozoic structural evolution and tectono-stratigraphic framework of the northern Gulf coast continental margin. *In:* Jackson, M.P.A.; Roberts, D.G., and Snelson, S. (eds.), *Salt tectonics: A Global Perspective*, *American Association of Petroleum Geologists Memoir 65*, 109–151.

Dixon, T.H.; Novali, F.; Rocca, F.; Dokka, R.; Sella, G.S.; Kim, W.; Wdowinski, S.; Whitman, D.; Amelung, F., and Ferretti, A., 2006. Space geodesy: Subsidence and flooding in New Orleans. *Nature*, 441, 587–588.

Dokka, R.K., 2006, Modern-day tectonic subsidence in coastal Louisiana. *Geology*, 34, 281–284.

Dokka, R.K., 2011. The role of deep processes in late 20th century subsidence of New Orleans and coastal areas of southern Louisiana and Mississippi. *Journal of Geophysical Research: Solid Earth*, 116, B06403. doi: 10.1029/2010JB008008

Dokka, R.K.; Sella, G.F., and Dixon, T.H., 2006. Tectonic control of subsidence and southward displacement of southeast Louisiana with respect to stable North America. *Geophysical Research Letters*, 33(23), L23308.

Ellwood, B.B.; Balsam, W.L., and Roberts, H.H., 2006. Gulf of Mexico sediment sources and sediment transport trends from magnetic susceptibility measurements of surface samples. *Marine Geology*, 230(3–4), 237–248.

Ewing, T.E. and Galloway, W.E., 2019. Evolution of the Northern Gulf of Mexico Sedimentary Basin. *The Sedimentary Basins of the United States and Canada,* 627–694.

Fisk, H.N., 1948. Geological investigation of the lower Mermentau river basin and adjacent areas in coastal Louisiana. *U.S. Army Corps of Engineers, Mississippi River Commission, Vicksburg, Mississippi,* 8–37.

Fisk, H.N. and McClelland, B., 1959. Geology of the continental shelf off Louisiana: Its influence on offshore foundation design. *Geological Society of America Bulletin*, 70, 1360–1394.

Fisk, H.N., and McFarlan, E., 1955. Late Quaternary deltaic deposits of the Mississippi River. *Geological Society of America Special Paper*, 62, 297–302.

Frank, J.P., 2017. Evidence of Fault Movement during the Holocene in Southern Louisiana: Integrating 3-D Seismic Data with Shallow High Resolution Seismic Data. New Orleans, Louisiana: University of New Orleans, Master's thesis, 91p.

Frank, J.P. and Kulp, M.A., 2016. Integrating 3-D industry seismic with shallow, high-resolution seismic: Have deep-seated faults affected Pleistocene through Holocene environments of south Louisiana. *Geological Society of America Abstracts with Programs*, 48(7).

Gagliano, S.M., 2005. Effects of natural fault movement on land subsidence in coastal Louisiana. *Proceedings of the 14th Biennial Coastal Zone Conference* (New Orleans, Louisiana).

Gagliano, S.M.; Kemp, E.B.; Wicker, K.M., and Wiltenmuth, K.S., 2003a. Fault related subsidence and land submergence in southern Louisiana. *American Association of Petroleum Geologists Annual Meeting* (Salt Lake City, Utah), 90013.

Gagliano, S.M.; Kemp, E.B.; Wicker, K.M.; Wiltenmuth, K., and Sabate, R.W., 2003b. Neo-tectonic framework of the southeast Louisiana and applications to coastal restoration. *Transactions of the Gulf Coast Association of Geological Societies*, 53, 262–272.

Galloway, W.E., 2008. Depositional evolution of the Gulf of Mexico sedimentary basin. *Sedimentary Basins of the World*, 5, 505–549.

González, J.L. and Törnqvist, T.E., 2006. Coastal Louisiana in crisis: Subsidence or sea level rise? *EOS, Transactions of the American Geophysical Union,* 87(45), 493–498.

Gosselink, J.G.; Cordes, C.L., and Parsons, J.W., 1979. An ecological characterization study of the Chenier Plain coastal ecosystem of Louisiana and Texas. *U.S. Fish and Wildlife Service, Office of Biological Sciences*. FWS/OBS-78/9 through 78/11.

Gould, H.R. and McFarlan, E., 1959. Geologic history of the Chenier Plain, southwestern Louisiana. *Transactions of the Gulf Coast Association of Geological Societies*, 9, 261–270.

Heinrich, P.V., 2006. *White Lake 30 × 60 Minute Geologic Quadrangle*. Baton Rouge: Louisiana Geological Survey, scale 1:100,000, 1 sheet.

Heltz, J.O., 2005. Evidence of Neotectonic Activity in Southwest Louisiana. Baton Rouge, Louisiana: Louisiana State University, Master's thesis, 90p.

Hijma, M.P.; Shen, Z.; Törnqvist, T.E., and Mauz, B., 2017. Late Holocene evolution of a coupled, mud-dominated delta plain–chenier plain system, coastal Louisiana, USA. *Earth Surface Dynamics*, 5(4), 689.

HIS Kingdom, 2019. *HIS Kingdom: Seismic and Geological Interpretation Software*. https://ihsmarkit.com/products/kingdom-seismic-geological-interpretation-software.html

Howe, H.V.; Russell, R.J., and McGuirt, J.H., 1935. Physiography of coastal southwest Louisiana. *Louisiana Geological Survey Bulletin*, 6, 1–68.

Hoyt, J.H., 1969. Chenier versus barrier, genetic and stratigraphic distinction. *American Association of Petroleum Geologists Bulletin*, 53(2), 299–305.

Jankowski, K.L.; Törnqvist, T.E., and Fernandes, A.M., 2017. Vulnerability of Louisiana's coastal wetlands to present-day rates of relative sea-level rise. *Nature Communications*, 8, 14792.

Johnston, A.; Zhang, R.; Gottardi, R., and Dawers, N.H., 2017. Investigating the relationship between tectonics and land loss, near Golden Meadow, Louisiana by utilizing 3D seismic and well log data. *Geological Society of America Abstracts with Programs*, 49(6).

Jones, C.E.; An, K.; Blom, R.G.; Kent, J.D.; Ivins, E.R., and Bekaert, D., 2016. Anthropogenic and geologic influences on subsidence in the vicinity of New Orleans, Louisiana. *Journal of Geophysical Research: Solid Earth*, 121(5), 3867–3887.

Kuecher, G.J., 1994. Geologic Framework and Consolidation Settlement Potential of the Lafourche Delta, Topstratum Valley Fill; Implications for Wetland Loss in Terrebonne and Lafourche Parishes, Louisiana. Baton Rouge, Louisiana: Louisiana State University, Ph.D. dissertation, 375p.

Kuecher, G.J., 1995. The dominant processes responsible for subsidence of coastal wetlands in south Louisiana, in Land Subsidence. *Proceedings of the Fifth International Symposium on Land Subsidence*, 69–81.

Kuecher, G.J.; Roberts, H.H.; Thompson, M.D., and Matthews, I., 2001. Evidence for active growth faulting in the Terrebonne delta plain, south Louisiana: Implications for wetland loss and the vertical migration of petroleum. *Environmental Geosciences*, 8(2), 77–94.

Kulp, M.A., 2000. Holocene Stratigraphy, History, and Subsidence of the Mississippi River Delta Region, North-Central Gulf of Mexico. Lexington, Kentucky: University of Kentucky, Master's thesis, 336p.

Kulp, M.; Howell, P.; Adiau, S.; Penland, S.; Kindinger, J., and Jeffress, W.S., 2002. Latest quaternary stratigraphic framework of the Mississippi River delta region. *Transactions of the Gulf Coast Association of Geological Societies*, 52, 573–582.

Louisiana State University (LSU): Department of Geography and Anthropology. *Cartographic information center*. https://www.lsu.edu/ga/labs/cartographic.php

McBride, R.A.; Taylor, M.J., and Byrnes, M.R., 2007. Coastal morphodynamics and Chenier Plain evolution in southwestern Louisiana, USA: A geomorphic model. *Geomorphology*, 88(3–4), 367–422.

McCulloh, R.P. and Heinrich, P.V., 2012. Surface faults of the south Louisiana growth-fault province. *In:* Cox, R.T; Tuttle, M.P.; Boyd, O.S., and Locat, J. (eds.), *Recent Advances in North American Paleoseismology and Neotectonics east of the Rockies and Use of the Data in Risk Assessment and Policy*. *Geological Society of America Special Paper 493*, 37–49.

McLean, C.M., 1957. Miocene geology of southeastern Louisiana. *Transactions of the Gulf Coast Association Geological Societies*, 7, 241–45.

Meckel, T.A., 2008. An attempt to reconcile subsidence rates determined from various techniques in southern Louisiana. *Quaternary Science Reviews*, 27(15–16), 1517–1522.

Meckel, T.A.; ten Brink, U.S., and Williams, S.J., 2007. Sediment compaction rates and subsidence in deltaic plains, numerical constraints and stratigraphic influences. *Basin Research*, 19(1), 19–31.

Milliken, K.T.; Anderson, J.B., and Rodriguez, A.B., 2008. Tracking the Holocene evolution of Sabine Lake through the interplay of eustasy, antecedent topography, and sediment supply variations, Texas and Louisiana, USA. *In:* Anderson, J.B. and Rodriguez, A.B. (eds.), *Response of Upper Gulf Coast Estuaries to Holocene Climate Change and Sea-Level Rise*. *Geological Society of America Special Paper 443*, 65–88.

Morton, R.A.; Bernier, J.C.; Barras, J.A., and Ferina, N.F., 2005. Rapid subsidence and historical wetland loss in the Mississippi Delta plain: Likely causes and future complications, Terrebonne Parish, Louisiana. Open File Report 2005-1216. *US Department of the Interior, US Geological Survey*, 116p.

Murray, G. E., 1961. *Geology of the Atlantic and Gulf coastal province of North America*. New York, Harper and Bros., 692p.

Nicol, A.; Watterson, J.; Walsh, J.J., and Childs, C., 1996. The shapes, major axis orientations and displacement patterns of fault surfaces. *Journal of Structural Geology*, 18(2–3), 235–248.

Nienhuis, J.H.; Törnqvist, T.E.; Jankowski, K.L.; Fernandes, A.M., and Keogh, M.E., 2017. A new subsidence map for coastal Louisiana. *Geological Society of America Today*, 27, 58–59.

O'Leary, M., 2018. Relationship between Growth Fault and Subsidence: Impact on Coastal Erosion, an Example from Cameron Prairie, Southwestern Louisiana. Lafayette, Louisiana: University of Louisiana at Lafayette, Master's thesis, 104p.

Owen, D.E., 2008. Geology of the Chenier Plain of Cameron Parish, southwestern Louisiana. *In:* Moore, G. (ed.), *Geological Society of America Field Guide 14, 2008 Joint Annual Meeting* (Houston, Texas), 27–38.

Penland, S. and Suter, J.R., 1989. The geomorphology of the Mississippi River chenier plain. *Marine Geology*, 90(4), 231–258, 243–258.

Russell, R.J. and Howe, H.V., 1935. Cheniers of southwestern Louisiana. *Geographical Review*, 25(3), 449–461. doi:10.2307/209313

Salvador, A., 1987. Late Triassic-Jurassic paleogeography and origin of Gulf of Mexico Basin. *American Association of Petroleum Geologists Bulletin*, 71(4), 419–451.

Scates, A. and Zhang, R., 2019. Locating faults in Louisiana Gulf Coast Quaternary stratigraphy by combination of cone penetrometer tests with borings and chirp seismic data, Golden Meadow, Louisiana. *GeoGulf Transactions*, 69, 415–420.

Shen, Z.; Dawers, N.H.; Törnqvist, T.E.; Gasparini, N.M.; Hijma, M.P., and Mauz, B., 2017. Mechanisms of late Quaternary fault throw-rate variability along the north central Gulf of Mexico coast: Implications for coastal subsidence. *Basin Research*, 29(5), 557–570.

State of Louisiana Department of Natural Resources (DNR). http://www.dnr.louisiana.gov/

Strategic Online Natural Resources Information System (SONRIS). *Access data*. http://www.sonris.com/

Tearpock, D.J. and Bischke, R.E., 2002. Applied Subsurface Geological Mapping with Structural Methods. Upper Saddle River, New Jersey: Prentice-Hall, 864p.

Törnqvist, T.E.; Bick, S.J.; van der Borg, K., and de Jong, A.F.M., 2006. How stable is the Mississippi Delta? *Geology*, 34(8), 697–700.

Törnqvist, T.E.; Wallace, D.J.; Storms, J.E.A.; Wallinga, J.; van Dam, R.L.; Blaauw, M.; Derksen, M.S.; Klerks, C.J.W.; Meijneken, C., and Snijders, E.M.A., 2008. Mississippi Delta subsidence primarily caused by compaction of Holocene strata. *Nature Geoscience*, 1, 173–176.

Twilley, R.R.; Bentley, S.J.; Chen, Q.; Edmonds, D.A.; Hagen, S.C.; Lam, N.S.N.; Willson, C.S.; Xu, K.; Braud, D.; Peele, R.H., and McCall, A., 2016. Co-evolution of wetland landscapes, flooding, and human settlement in the Mississippi River Delta Plain. *Sustainability Science*, 11(4), 711–731.

Van Andel, T.H., 1960. Sources and dispersion of Holocene sediments, northern Gulf of Mexico. *American Association of Petroleum Geologists Bulletin,* Special Volume 21, 34–55.

Wolstencroft, M.; Shen, Z.; Törnqvist, T.E.; Milne, G.A., and Kulp, M., 2014. Understanding subsidence in the Mississippi Delta region due to sediment, ice, and ocean loading: Insights from geophysical modeling. *Journal of Geophysical Research: Solid Earth*, 119(4), 3838–3856.

Worrall, D.M. and Snelson, S., 1989. Evolution of the northern Gulf of Mexico. *In:* Bally, A.W. and Palmer A.R. (eds.), *The Geology of North America—An overview. Geological Society of America, Geology of North America*, A, 97–138.

Yang, S.Y, 1992. Structure and Stratigraphy of West and East Cameron and Neighboring OCS Areas, Offshore Western Louisiana, Gulf of Mexico. College Station, Texas: Texas A&M University, Ph.D. dissertation, 111p.

Yeager, K.M.; Brunner, C.; Kulp, M.A.; Fischer, D.; Feagin, R.A.; Schindler, K.J.; Prouhet, J., and C. Gopal, 2012. Significance of active growth faulting on marsh accretion processes in the lower Pearl River, Louisiana. *Geomorphology*, 153–154, 127–143.

Young, S.C.; Ewing, T.; Hamlin, S.; Baker, E., and Lupin, D., 2012. Updating the hydrogeologic framework for the northern portion of the Gulf Coast Aquifer (final report). *Texas Water Development Board*, 283p. https://texashistory.unt.edu/ark:/67531/metapth542209/; http://www.twdb.texas.gov/publications/reports/contracted_reports/doc/1004831113_GulfCoast.pdf

Yu, S.-Y.; Törnqvist, T.E., and Hu, P., 2012. Quantifying Holocene lithospheric subsidence rates underneath the Mississippi Delta. *Earth and Planetary Science Letters*, 331–332, 21–30.

Yuill, B.; Lavoie, D., and Reed, D.J., 2009. Understanding subsidence processes in coastal Louisiana. *In:* FitzGerald, D. and Reed, D.J. (eds.), *Geologic and Environmental Dynamics of the Pontchartrain Basin. Journal of Coastal Research,* Special Issue 54, pp. 23–36.

Zou, L.; Kent, J.; Lam, N.; Cai, H.; Qiang, Y., and Li, K, 2015. Evaluating land subsidence rates and their implications for land loss in the lower Mississippi River basin. *Water*, 8(1), 10.